DOI: 10.1002/ ((please add manuscript number))
Article type: Full Paper

Aminal/Schiff-Base Polymer to N-doped Porous Carbon Nanospheres for High-Performance Supercapacitor

Fei Li[1], Xinhua Huang[*,1], Nuoya Wang[1], Xingxing Zhu[1], Vincent Chan[2], Ruikun Zhao[3], Yimin Chao*[*,4]*

F. Li, Dr. X. Huang, N. Wang, X. Zhu
School of Materials Science and Engineering, Anhui University of Science and Technology, Huainan, Anhui, 232001, P. R. China
The Key Laboratory of Functional Molecular Solids, Ministry of Education, Anhui Normal University, Wuhu, Anhui, 232001, P. R. China
E-mail: xhhuang@aust.edu.cn
Dr. V. Chan, Prof.
Department of Biomedical Engineering, Khalifa University, Abu Dhabi 127788, UAE
Dr. R. Zhao
College of Arts and Sciences, Khalifa University of Science and Technology, PO Box 127788, Abu Dhabi, UAE

Dr. Y. Chao,

School of Chemistry, University of East Anglia, Norwich, NR4 7TJ, UK

E-mail: Y.Chao@uea.ac.uk

Keywords: aminal bonding, activation, nanosphere, porous carbon, supercapacitor

Abstract: In this study, the polymer containing aminal and imine (C=N) linkages was synthesized from the reaction between p-phthalaldehyde and 2,6-diaminepyridine through nucleophilic addition. Subsequently, nitrogen-doped carbon nanospheres (N-CNS) were fabricated by a process of sequential potassium hydroxide (KOH) activation and direct carbonization of the polymer. Interestingly, mass ratio (x) of polymer to KOH was found to play a crucial role in dictating the porosity, surface chemistry and capacitive performance of the resulted carbon nanoparticles. The optimization of x led to the formation of N-CNS-2 with significantly larger specific surface area (809 m^2 g^{-1}, 98% microporous content) and highest specific capacitance (732 F g^{-1}) at 8 A g^{-1} in 6 M KOH aqueous electrolyte. In addition, the electrode fabricated with N-CNS-2 showed an excellent cycling stability along with 98% of

the initial specific capacitance after 5000 charge/discharge cycles. The carbon precursor with aminal linkages network has shown very promising potential in the energy storage materials.

1. Introduction

Owing to the advantages of porous carbon (PC), such as superior electricity storage, low price, long life service and high stability, 80% of the electrode materials of electrochemical double layer capacitors (EDLC) are composed of PC.[1-4] Many efforts have focused on tailoring the morphology,[5] doping elements,[6,7] surface area and pore structure[8,9] of PC in order to elevate the performance of EDLC electrodes. Different classes of PC have been derived from biomass[10-12] and wastes[13-15] by specific chemical activations under certain conditions, demonstrating great potentials as the electrode material in energy-storage device. On the other hand, most common PC possess far from ideal electrochemical properties for EDLC applications due to the limitations by the diversity of raw materials, intricate processing conditions and environmental influence, which often lead to confounded physical characteristics such as high current leakage.[16]

Recently, various classes of synthetic polymeric materials including triazine network, conjugated polymer, hyper-crosslinked polymer, and covalent organic frameworks have been developed from highly controllable synthesis and structure, which can be potentially applied as novel PC precursors.[17-20] Especially, conducting polymer based carbon materials have been well applied for the supercapacitors.[17,18] Among several popular approaches, original nitrogen-doped carbon has been synthesized from triazine polymer,[21-24] secondary amine polymer,[25,26] hexamine polymer[27] or Schiff-base polymer,[28-31], leading to the optimization of the carbon materials' pseudo-capacitance, wettability, and surface area, which is paving the most promising way for the development of superior carbon electrodes. However, nitrogen atoms in most polymer precursors are released from the bulk material during pyrolysis at high temperature because the usual low-band-energy of C-N bonds (305 kJ mol^{-1}), leading to low

nitrogen content in the resulted PC. In order to increase the nitrogen content of PC, highly energized C=N bonds (615 kJ mol^{-1}) have been introduced in the polymer matrix for preventing N atoms from leaving the bulk material during pyrolysis. For examples, new class of polymer containing Schiff base or C=N groups within the material bulk has been developed.[32-34,24] On the other hand, evolving new nitrogen-containing linkage polymer is still one of the driving forces to push the field forward. Aminal-linkage and the N, N-acetal are strong enough in the polymer structure.[35,36] To best of our knowledge, few of reported data has applied it into carbon precursor.

Inspired by the advantages of C=N and aminal bond in N-doped PC synthesis, we have developed a new strategy for the design of nitrogen functionalized polymeric precursors and fabrication of highly nitrogen-doped porous carbon nanospheres (N-CNSs). In our unique strategy, 2,6-diaminopyridine was employed as the nitrogen sources of PC, carbon-rich p-phthalaldehyde was incorporated during one-pot polycondensation of the p-phthalaldehyde with 2,6-diamnopyridine and finally formation of Schiff base and aminal mixing structure polymers. Finally, the N-CNSs were obtained from the carbonization of the mixed polymers by pyrolysis under an activation step with KOH solution. The unique properties of N-CNSs prepared here include: 1) the coexistence of intramolecular imine (C=N) and aminal bonds in the polymer precursor aids to maintain the nitrogen content in the resulted PC from pyrolysis (Figure 1); 2) excellent electrochemical performances stemmed from the high engineered surface area, abundant microporous structure and high nitrogen dopant of N-CNS.

2 Results and discussion

2.1 Synthetic Route and Bond Analysis

The synthetic route of N-CNS is presented in Figure 1. Firstly, the condensation between 2,6-diamnopyridine and p-phthalaldehyde leads to the formation of a nitrogen-rich polymer.

Figure S1 shows the solid-state ^{13}C NMR spectrum of the polymer. In general, the peaks at 171 ppm and 45 ppm are assigned to the carbon of imine group (C=N) and carbon covalently linked to secondary amine (-NH-CH-NH-) leading to aminal structure.[35] Moreover, the peak at 193 ppm corresponds to the residual aldehyde end group (C=O) from terminal p-phthalaldehyde unit in the polymer and the signals between 116-149 ppm are assigned to the aromatic carbon.[37] From Figure S2, FT-IR spectrum confirms the formation of C=N linkage of the polymeric backbone with the emergence of characteristic peak at 1622 cm^{-1}, which validates that Schiff-base polymer was successfully synthesized. Also, the peak at 3450 cm^{-1} is ascribed to the vibrational mode of $-NH_2$ or -NH in the skeleton of polymer. The results obtained herein agrees well with other similar polymers, confirming the formation of Schiff base and aminal bonds in the polymer herein.[38]

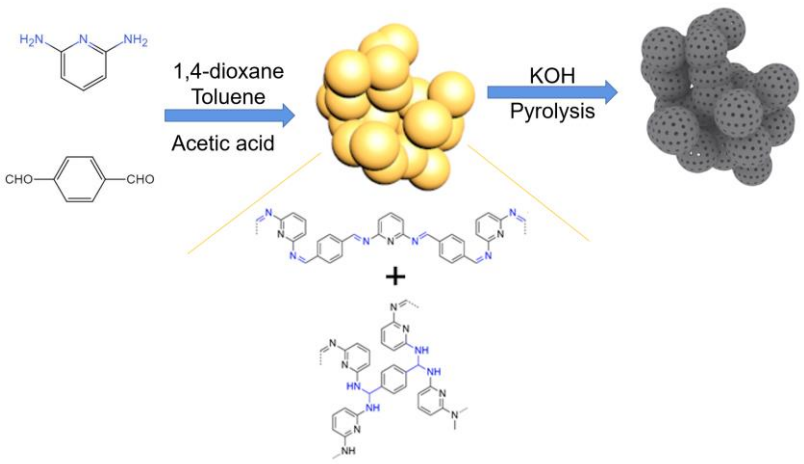

Figure 1 Schematic synthesis route of N-CNS from the aminal and imine (C=N) linkages polymer followed by KOH activation

2.2 Structure and Morphological Analysis

Raman spectra demonstrate that N-CNSs exhibit two main peaks at 1346 cm^{-1} and 1587 cm^{-1} denoted as D band and G band, respectively (Figure 2a). The intensity ratio of D band to G band (I_D/I_G) of the four specimens ranges from 0.93 to 1.04, which indicate that N-CNSs increased degree of graphitization due to the KOH/N-CNS precursor ratio (Figure 2a).[39,40] Figure 2b shows the XRD spectrum of N-CNSs displaying two major peaks at 25° and 42°,

The broad but well-defined diffraction peak at 25° suggests the partially graphitic nature for the carbon derived directly from polymer, representing the characteristics of amorphous structure of carbon-based materials. Moreover, N_2 adsorption-desorption isotherms of N-CNSs are shown in Figure 3a. The result indicates that N-CNS without going through KOH activation shows minimum adsorption capacity among all four samples while N-CNS-1, N-CNS-2, and N-CNS-3 provide effective adsorption capacity. KOH decomposes during the calcination process and reacts with carbon materials to generate CO_2 and other gases, which is the cause of the voids. The carbon atoms linked with N are also lost during the reaction of the KOH etching carbon framework. Therefore, KOH plays a vital important role in the formation of porous structure during the pyrolysis of nitrogen-rich polymer. Interestingly, N_2 isotherm of each KOH activated N-CNS sample shows type I behaviour with a sharp increase of adsorption capacity when P/P_0 increases from 0 to 0.05, indicating the presence of microporous solid with relatively small external surfaces. According to literature, the trend of surface area of N-CNS is increasing with the mass ratio of activated KOH increased.[41] In actual operation, when the mass ratio of polymer to KOH is 3, the muddy like mixture indicates all the KOH used to activate the polymer in the pyrolysis process. When the ratio is 2, the semi-mud mixture indicates some KOH lost before activation. When the ratio is 1, even though the highest ratio KOH used, but the suspension mixture means a lot of KOH lost before the activation. Therefore, the surface area of N-CNS-3 is the highest, but it's similar to N-CNS-1, while the samples N-CNS-2 is the worst.

The structural feature as mentioned above is further supported by the pore size distribution curves (Figure 3b) and the averaged pore size of 1.76 nm among the three N-CNS samples (Table 1). The narrower pore size distribution of N-CNSs leads to significantly larger percentage of microporous surface area above 97% (e.g., 3% external surface area) compared to N-CNS, ascribed to the formation of porous network with different cavities upon the polycondensation between p-phthalaldehyde and 2,6-diaminopyridine through the establishment of aminal linkages.[42]

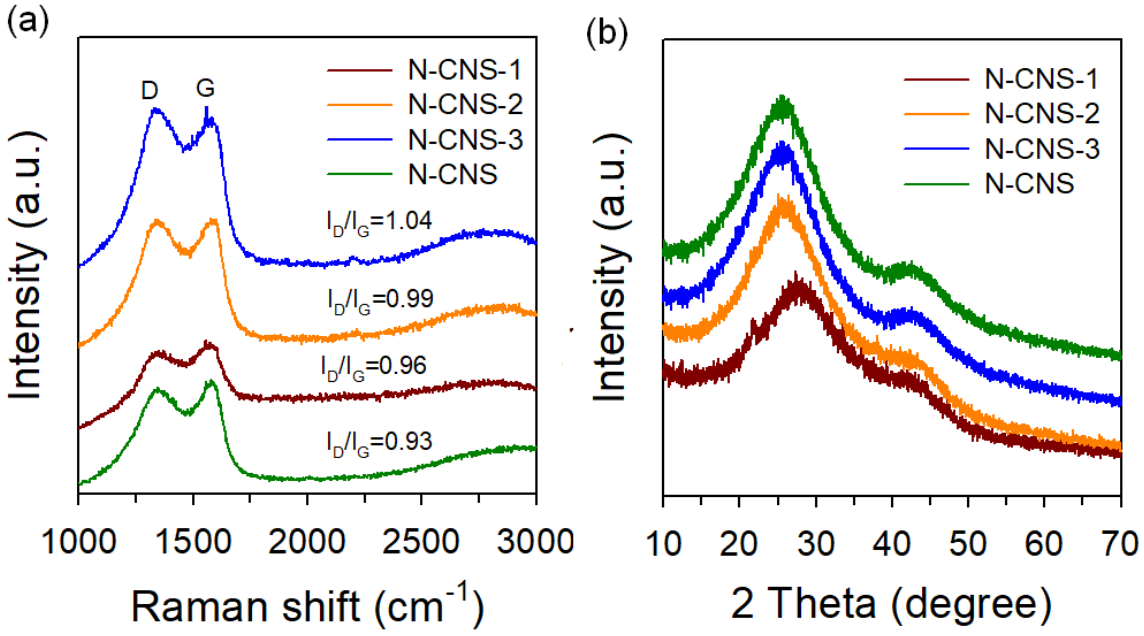

Figure 2 (a) The Raman spectra of the N-CNSs; (b) XRD diffraction pattern of N-CNSs.

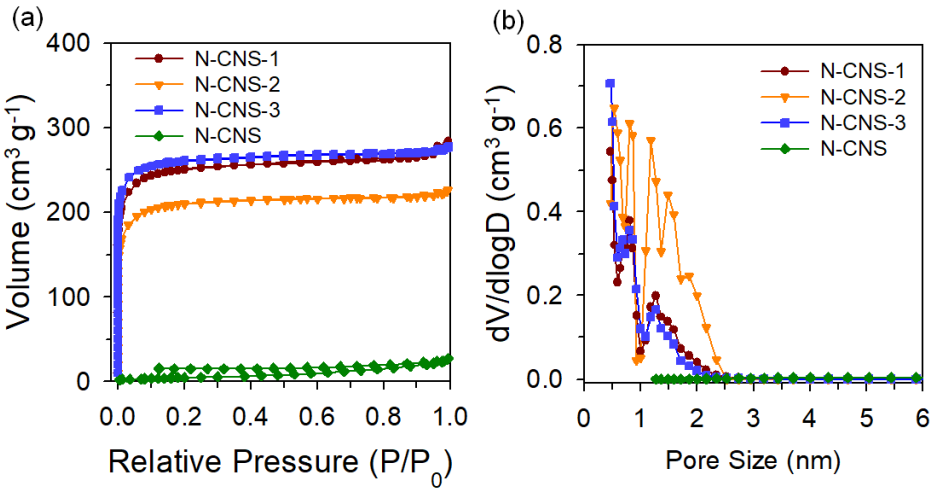

Figure 3 (a) N_2 adsorption-desorption isotherms of the N-CNSs; (b) The pore size distribution of the N-CNSs.

Table 1 Pore structure parameters of N-CNS

Samples	S_{BET} ($m^2 g^{-1}$)	S_{micro} ($m^2 g^{-1}$)	S_{micro}/S_{BET} %	V_{total} ($cm^3 g^{-1}$)	Pore size (nm)
N-CNS	19.66	2.48	12.6	0.04	8.55
N-CNS-1	973.79	954.88	98.1	0.44	1.80
N-CNS-2	809.91	795.46	98.2	0.35	1.73
N-CNS-3	1025.17	996.79	97.2	0.43	1.67

The surface morphologies of the N-CNSs with or without KOH activation are investigated by SEM and TEM technology. As shown in Figure 4 and Figure S3, the overall morphologies of the obtained carbon samples are maintained aggregated spheres. Interestingly, the diameter and overall morphologies of the microsphere is not altered by KOH activation during pyrolysis and carbonization. The general feature of agglomerated micro-particles was similar to that of other types of microporous materials,[43] which are considered as prime candidate for the energy storage application in supercapacitors.[44] The TEM images in Figure S4 show solid spheres with microporous at the spheres surface.

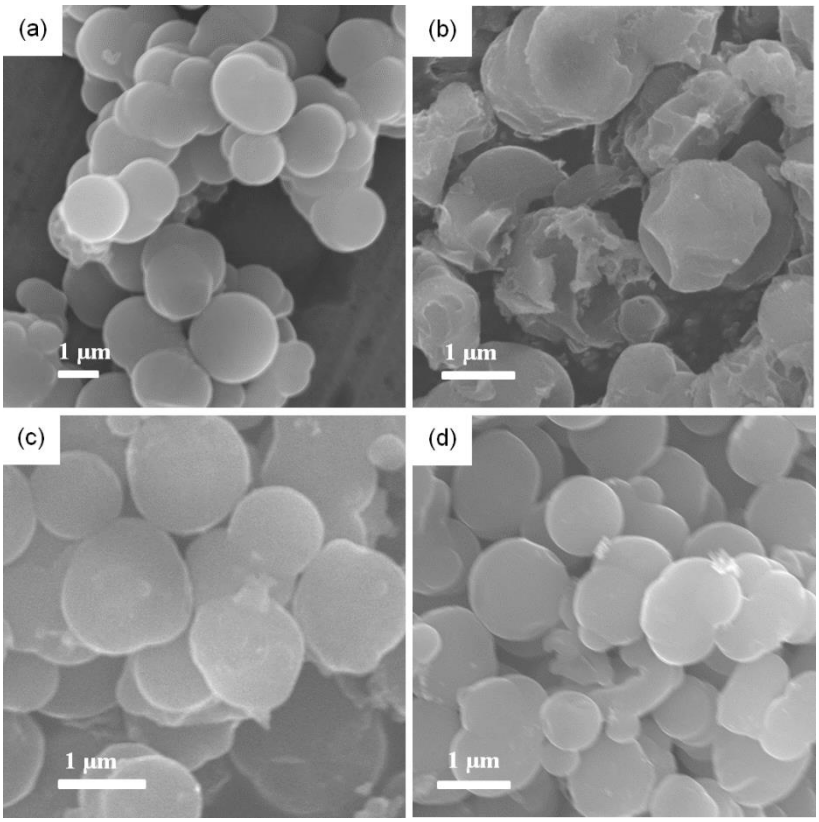

Figure 4 SEM images of the N-CNS activated by different mass of KOH: a) N-CNS without activated; b) N-CNS-1; c) N-CNS -2; d) N-CNS -3.

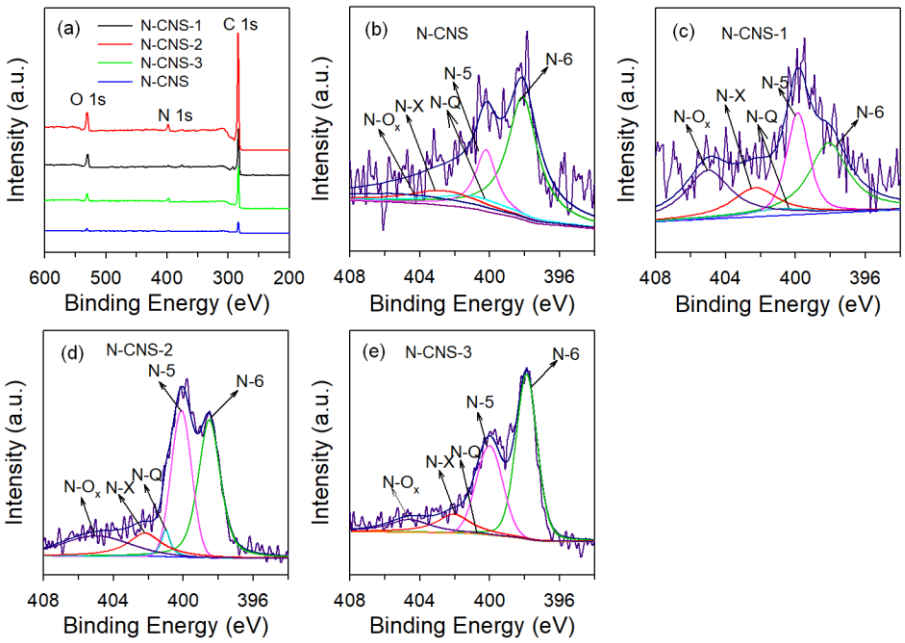

Figure 5 The XPS survey spectrum (a) and core level N1s spectra of N-CNSs (b-e).

Wide scan XPS spectra of N-CNSs shows that C1s, N1s and O1s peaks locate at 285.1, 400, 533.1 eV, respectively (Figure 5). The oxygen content of N-CNSs is likely originated from the residual aldehyde groups and adsorbed H_2O vapor residing in the nanopores of carbon-based matrix. The N1s spectrum of each sample can be deconvoluted into five peaks assigned to pyridine-N-6 (398.5 eV), pyridine-N-5 (400.1 eV), quaternary-N-Q (401.5 eV), pyridine-N-oxide (402.2 eV) or ammonia and chemisorbed nitrogen oxide-N-Ox (405.0 eV).[45] Table 2 summarizes the relative abundance of the five types of specific N species of N1s peak. Followed by an increase of KOH to polymer mass ratio prior to pyrolysis, the resultant nitrogen content of N-CNS increases from 3.42% to 5.16%. It is because that nitrogen in N-CNSs is stemmed from C-N single bond (the aminal linkages) and C=N (in pyridine) in the polymer precursor. Moreover, high nitrogen content is brought about by highly stable C=N bond (615 KJ mol^{-1}) maintained from the polymer precursor after carbonization. However, the carbon atoms linked with N are also lost during the reaction of the KOH etching carbon framework. More KOH added, the more N lost. Anyway, the nitrogen-doping in N-CNS for

application as electrodes not only improves the hydrophilic property but also enhances the pseudo-capacitance. Among all nitrogen species, pyridinic nitrogen and pyrrolic nitrogen mainly induces pseudo-capacitance, while pyridine N-oxide likely promote ion transport and increase specific capacitance.

Table 2 Elemental compositions of C, N and O, and relative content of N species to N1s in N-CNSs.

Sample	C (at%)	O (at%)	N (at%)	N-6 (%), 398.5 eV	N-5 (%), 400.1 eV	N-Q (%), 401.0 eV	N-X (%), 402.2 eV	N-Ox (%), 405.0 eV
N-CNS-1	83.77	12.81	3.42	31.4	22.5	5.2	15.6	25.3
N-CNS-2	87.51	8.03	4.46	37.9	30.5	3.6	12.2	15.8
N-CNS-3	90.61	4.23	5.16	48.30	29.4	0.20	12.2	9.90
N-CNS	86.21	10.07	3.72	44.8	15.8	12.3	12.7	14.4

2.3 Supercapacitive Properties

The CVs of various types of N-CNS electrodes in a two-electrode system at 100 mV s^{-1} appears rectangular in shape, indicating the attainment of high charge transfer rate and ideal EDLC capacitance (Figure 6). On the other hand, high nitrogen content in N-CNSs which contributes to the high pseudo-capacitance leads to the disappearance of oxidation and reduction peaks in the CV scan even under high scan rate (Figure S5).[46] Moreover, the highest enclosed integral area implies of N-CNS-2 among all samples test herein implies most significant capacitance (Figure 6a).

To further evaluate the electrochemical property of N-CNS electrodes, the GCD measurements for all the electrodes were carried out. GCD curves of all samples at 8 A g^{-1} are shown in Figure 6b, the capacitance of N-CNS electrodes calculated according to the GCD curves decrease in the following order: N-CNS-2 (732 F g^{-1}) > N-CNS-1 (460 F g^{-1}) > N-CNS-3 (448 F g^{-1}) > N-CNS (222 F g^{-1}). The GCD result validates that N-CNS-2 achieves the highest capacitance among all samples. The main factors to determine the specific capacitance for electrode materials are: (1) the specific surface area; (2) Pore structure including pore size and distribution; (3) suitable kinds and ratio elements doped. Usually, the electrode materials capacitance performance is the collective effect of all the above factors.[47,48] According to the surface analysis, N-CNS-2 possesses the largest micropores ratio and suitable O, N elements content that because a too high element-doping level (> 10.0 at%) usually causes many defect

sites, deteriorating the electrical conductivity and rate performance.[46][49] In addition, materials with high specific surface area originating from tortuous and dead-end micropores leads to the poor performance of electrodes with difficulty for the fabrication of practical electrodes. It is worth noting that at lower current density, such as at 5 A g^{-1}, N-CNS electrodes have the higher specify capacitance, but their rate performance is obviously declined, mainly related to the internal resistance.[50] From Figure S6, it is shown that the N-CNS, N-CNS-1, and N-CNS-2 have the mutation potential at the moment of charge and discharge conversion because of their internal resistance,[51,52] leading to the discharge time longer than the charge time according to the following equation:

$$R = \Delta\varphi/2i \quad (1)$$

where R is the equivalent series internal resistance (**Ω**), i is the charge-discharge current and Δφ is the mutation potential. Therefore, the overcoming of the internal resistance at a lower current can influence the performance of N-CNS electrodes (Figure S6). The trend of specific capacitances as a function of current density is present in Figure 6c, as calculated by their GCD test with equation (2). The results indicate that all electrodes have the good rate performance at the current density from 8 A g^{-1} to 20 A g^{-1} (above 77.5%). For example, N-CNS-3 electrode has attained specific capacity of 416 F g^{-1} at 20 A g^{-1} (93% of 448 F g^{-1} at 8.0 A g^{-1}).

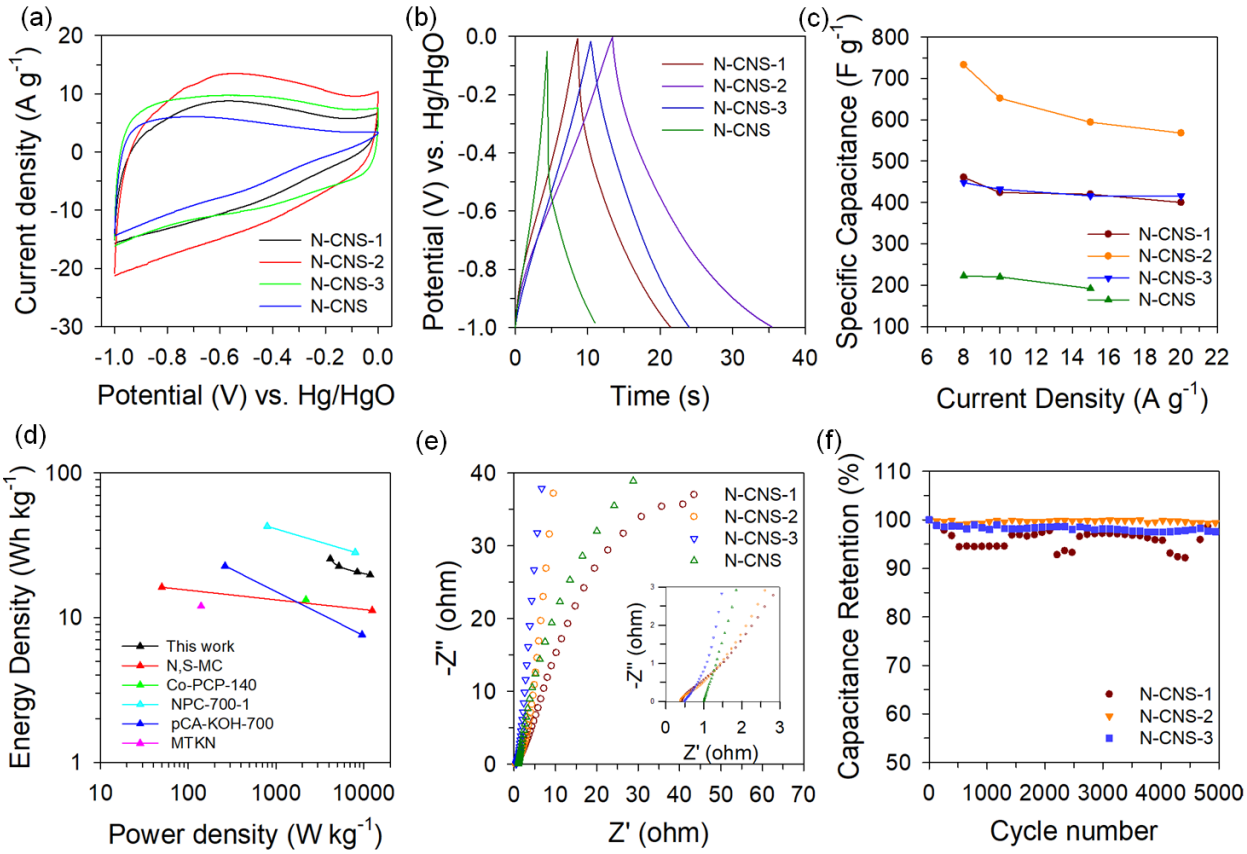

Figure 6 (a) The CV of N-CNSs at the scan rate of 100 mV s^{-1}; (b) The GCD N-CNSs at the current density of 8 A g^{-1}; (c) The relationship between the specific capacitance and current density; (d) The Ragone plots of N-CNS-2 in this work, and N, S-MC,[53] Co-PCP-140,[54] NPC-700-1,[55] pCA-KOH-700,[56] MTKN[57] for comparison; (e) EIS of N-CNSs. (f) Cycle life of capacitance retention of the N-CNS-1, 2 and 3 at the current density of 10 A g^{-1}.

Moreover, Ragone plots of all the N-CNSs based electrodes showed good energy density stability (Figure S7), e.g., the highest energy density of N-CNS-2 electrode reaches 25.44 Wh kg^{-1} at a power density of 4156 W kg^{-1} at 8 A g^{-1}. Compared to other reported data, the N-CNS electrodes obviously demonstrate superiority of high energy density (Figure 6d).

Electrochemical impedance spectroscopy (EIS) is further applied to measure the equivalent series resistance (ESR), which is the sum of internal resistance of the electrode material, ionic resistance of KOH electrolyte and contact resistance between the electrode and graphite electrode. As shown in Figure 6e, the ESR value of KOH activated N-CNSs electrodes are

smaller than 1 Ω (the ESR of direct pyrolysis N-CNS is 1 Ω), indicating good conductivity from high level N-CNSs attached by KOH activation during pyrolysis. For practical applications, the long cyclic life is an important parameter for supercapacitor electrodes. GCD cycling was conducted to investigate the stability of KOH activated N-CNS-1, 2 and 3 electrodes. As shown in Figure 6f, except for N-CNS-1 showing some fluctuations, the N-CNS-2 and N-CNS-3 remains to have retention of 98% capacitance after 5000 cycles, showing good cycle stability and durability.

3 Conclusions

In summary, this study firstly demonstrated that nitrogen-rich polymeric precursors with aminal-linkage and Schiff base were synthesized from the 2,6-diaminopyridine and p-phthalaldehyde. Afterwards, nitrogen doped carbon-based microspheres (N-CNSs) were produced by activation with different amounts of KOH in order to engineer the best carbon-based materials with superior electrochemical properties. By this way, high nitrogen content (5.16 wt%) was successfully incorporated into N-CNSs with high surface area (up to 1025 m^2 g^{-1}) and abundant micro-/meso- porous structure (> 97%). N-CNSs as the EDLC electrodes demonstrated high-performance specific capacitance (732 F g^{-1} at 8 A g^{-1}) and long cycle stability (retention above 90% after 5000 cycles). The two types of nitrogen containing groups in polymeric precursor presented a new strategy for the controlled synthesis of carbon-based nanomaterials with high nitrogen doping and highly engineered microstructure. The outstanding electrochemical performance demonstrated the potential use of N-CNSs electrode in supercapacitor with high-energy rate and long cycle life.

4. Materials and methods

4.1. Synthesis of N-doped Carbon Nanospheres (N-CNS):

All chemicals used herein are of analytical grade and commercially available. Firstly, 0.15 g of 2,6-diaminopyridine was added to a solvent mixture with 100 mL of toluene and 40 mL of 1,4-dioxane. Then the solution was stirred vigorously until 2,6-diaminopyridine was

completely dissolved and 0.5 g of p-phthalaldehyde was added. Afterwards, 30 mL of acetic acid was added as catalyst to the mixture, which was transferred into Teflon-lined autoclave, heated to 120 ℃, and maintained for three days. The product obtained herein was washed three times with N, N-dimethylformamide and dried at 80 ℃ in order to get polymer powder with organic Schiff bases. The powder as mentioned above was then immersed in a 10 wt% KOH solution for 30 min and dried at 80 ℃, and transferred to a tube furnace set at 450 ℃ (5 ℃ min^{-1}) for 1 h under nitrogen atmosphere, and then heated at 700 ℃ for 2 h to prepare nitrogen doped carbon nanospheres (labelled as N-CNS-x, where x is the mass ratio of polymer to KOH, finally got the N-CNS-1, 2, 3, respectively). The N-CNS-x samples were then washed rinsed by using deionized water in order to remove the excess bases. The sample obtained by the same procedure without adding potassium hydroxide was named N-CNS, as a control.

4.2 Materials characterizations

The sample morphology was characterized by a field-emission scanning electron microscope (JEOL JSM-7610FFEG-SEM). N_2 adsorption and desorption isotherms were achieved from a Micromeritics (ASAP 2460 4MP) at -196 ℃. Specific surface area and the pore volume were calculated using the Brumauer-Emmett-Teller (BET) method within P/P_0 = 0.05-0.25 and Dubinin-Radushkevich plot at P/P_0 = 0.995, respectively. The pore size distribution was obtained from the adsorption branches of the isotherms using non-local density functional theory (NLDFT) equilibrium model. X-ray photoelectron spectrometer (XPS, ESCALAB 250Xi, Thermo Fisher Scientific, USA) was utilized to analyze the surface characteristics of the samples. X-ray diffraction (XRD) measurements were conducted on a Smartlab SE diffractometer with Cu radiation (λ= 0.154 nm). Thermo Nicolet^{TM} iS50 spectroscopy was applied to obtain the Fourier-transform infrared (FT-IR) spectra. Raman (inVia^{TM}, Renishaw, Britan) spectrum under λ_{ex} = 512 nm laser excitation was conducted under 10 s exposure time

and excitation power of 20 mW, ^{13}C NMR was tested on a Bruker avance III 600M solid-state nuclear magnetic spectrometer in Switzerland.

4.3 Electrochemical measurement

All electrochemical measurements were performed on a CH760E electrochemical workstation, with three-electrode and two-electrode systems for probing the electrochemical performance. In the three electrodes system, a Pt sheet was used as a counter electrode with Hg/HgO as a reference electrode. Most importantly, the working electrode was prepared by coating 85 wt% of N-CNS, 15 wt% of PVDF, using NMP as a binder on a graphite sheet, and then dried in an oven at 80 ℃. Cyclic voltammetry (CV) and galvanostatic charge/discharge (GCD) tests were conducted within the potential window of -1.0 to 0 V using a 6 M KOH solution as the electrolyte. Electrochemical impedance spectroscopy (EIS) was performed between frequencies of 10^{-2} to 10^{5} Hz. The specific capacitance was calculated from the GCD curve. The electrochemical performance of the as prepared sample electrode was further tested using a two-electrode configuration. The calculation on the single electrode mass ratio capacitance was based on the galvanostatic charge/discharge (GCD) test with the formula given as below:

$$C=4\ (I\ \Delta t)/(m\ \Delta U) \qquad (2)$$

where I is the constant current in a constant current charge-discharge curve, m is the total mass of the electrode, Δt is the discharge time, and ΔU is the discharge voltage.

Supporting Information

Supporting Information is available from the Wiley Online Library or from the author.

Acknowledgements

This work was supported by the Key Project of Natural Science Research in Anhui Colleges and Universities (KJ2017A070), Anhui Province Natural Science Foundation Project (1908085ME157), and Anhui Province Selective Foundation of Innovation Project for Study

Abroad (2019LCX020), and Open project of the Key Laboratory of Functional Molecular Solids of the Ministry of Education (FMS201922).

Received: ((will be filled in by the editorial staff))

Revised: ((will be filled in by the editorial staff))

Published online: ((will be filled in by the editorial staff))

References

[1] E. E. Miller, Y. Hua, F, H. Tezel, *J. Energy storage* **2018**, 20, 30-40.

[2] Z. Li, T. Mendezmorales, M. Salanne, *Curr. Opin. Electrochem.* **2018**, 9, 81-86.

[3] Y. Wang, Y. Song, Y. Xia, *Chem. Soc. Rev.* **2016**, 45, 5925-5950.

[4] W. Raza, F. Ali, N. Raza, Y. Luo, K. H. Kim, J. Yang, S. Kumar, *Nano Energy* **2018**, 52, 441-473.

[5] M. Gupta, P. Singh, B. Bhattacharya, Y. M. Shulga, N. Y. Shulga, Y. Kumar, *Appl. Phys. A* **2019**, 125, 1-15.

[6] J. Pampel, T. Fellinger, *Adv. Energy Mater.* **2016**, 6, 1502389.

[7] J. Niu, R. Shao, M. Liu, Y. Zan, M. Dou, J. Liu, Z. Zhang, Y. Huang, F. Wang, *Adv. Funct. Mater.* **2019**, 29, 1905095.

[8] T. Wang, H. Li, S. Shi, T. Liu, G. Yang, Y. Chao, F. Yin, *Small.* **2017**, 13, 20, 1604182.

[9] L. Chen, B. Yan, J. Xu, C. Wang, Y. Chao, X. Jiang, G. Yang, *ACS Appl. Mater. Interfaces* **2015**, 7, 13934.

[10] Z. Bi, Q. Kong, Y. Cao, G. Sun, F. Su, X. Wei, X. Li, A. Ahmad, L. Xie, C. Chen, *J. Mater. Chem. A* **2019**, 7, 16028-16045.

[11] M. Sevilla, N. Diez, G. A. Ferrero, A. B. Fuertes, *Energy Storage Mater.* **2019**, 18, 356-365.

[12] M. Vijayakumar, A. B. Sankar, D. S. Rohita, T. N. Rao, M. Karthik, *ACS Sustain. Chem. Eng.* **2019**, 7, 17175-17185.

[13] H. Nguyen, M. J. Moghadam, H. Moayedi, *J. Mater. Cycles Waste Manag.* **2019**, 21, 1039-1051.

[14] C. Schneidermann, P. Otto, D. Leistenschneider, S. Grätz, C. Eßbach, L. Borchardt, *Beilstein J. Nanotechnol.* **2019**, 10, 1618-1627.

[15] Y. Zhu, S. Yuan, D. Bao, Y. Yin, H. Zhong, X. Zhang, *Adv. Mater.* **2017**, 29, 1603719.

[16] R. T. Ayinla, J. O. Dennis, H. M. Zaid, Y. K. Sanusi, F. Usman, L. L. Adebayo, *J. Clean. Prod.* **2019**, 229, 1427-1442.

[17] Q. Meng, K. Cai, Y. Chen, L. Chen, *Nano Energy* **2017**, 36, 268-285.

[18] Poonam, K. Sharma, A. Arora, S. K. Tripathi, *J. Energy Storage* **2019**, 21, 801-825.

[19] Y. Han, L. Dai, *Macromol. Chem. Phys.* **2019**, 220, 1800355.

[20] T. O. Magu, A. U. Agobi, L. Hitler, P. M. Dass, *J. Chem. Rev.* **2019**, 1, 19-34.

[21] N. Deka, R. Patidar, S. Kasthuri, N. Venkatramaiah, G. K. Dutta, *Mater. Chem. Front.* **2019**, 3, 680-689.

[22] X. Huang, N. Wang, F. Li, X. Zhu, K. Liao, V. Chan, L. Zhang, *New J. Chem.* **2019**, 43, 15892-15898.

[23] L. Li, F. Lu, R. Xue, B. Ma, Q. Li, N. Wu, *ACS Appl. Mater. Interfaces* **2019**, 11, 26355-26363.

[24] A. F. M. El-Mahdy, Y. Hung, T. H. Mansoure, H. Yu, S. T. Chen, W. Kuo, *Chem-Asian. J.* **2019**, 14, 1429-1435.

[25] P. Liu, J. Yan, Z. Guang, Y. Huang, X. Li, W. Huang, *J. Power Sources* **2019**, 424, 108-130.

[26] D. Zhu, Y. Wang, L. Gan, M. Liu, K. Cheng, Y. Zhao, X. Deng, D. Sun, *Electrochim. Acta* **2015**, 158, 166-174.

[27] J. Wang, H. Liu, H. Sun, H. Wei, H. Wang, X. Liu, B. Wei, *Carbon* 2018, 127, 85-92.

[28] B. Tang, L. Zheng, X. Dai, H. Chen, *J. Energy Storage* **2019**, 26, 100961.

[29] M. Zhou, X. Li, H. Zhao, J. Wang, Y. Zhao, F. Ge, Z. Cai, *J. Mater. Chem. A* **2018**, 6, 1621-1629.

[30] Y. Li, L. Liu, Y. Wu, T. Wu, H. Wu, Q. Cai, Y. Xu, B. Zeng, C. Yuan, L. Dai, *J. Mater. Chem. A* **2019**, 7, 13154-13163.

[31] S. K. Das, K. Bhunia, A. Mallick, A. Pradhan, D. Pradhan, A. Bhaumik, *Micropor. Mesopor. Mat.* **2018**, 266, 109-116.

[32] X. Li, F. Deng, J. Li, Z. Li, F. Kang, *Electrochim. Acta* **2018**, 284, 355-365.

[33] W. Yang, L. Hou, X. Xu, Z. Li, X. Ma, F. Yang, Y. Li, *Carbon* **2018**, 130, 325-332.

[34] C. Cai, Y. Zou, C. Xiang, H. Chu, S. Qiu, Q. Sui, F. Xu, L. Sun, A. Shah, *Appl. Surf. Sci.* **2018**, 40, 47-54.

[35] S. Jiang, S. Gan, X. Zhang, H. Li, Q. Qi, F. Cui, J. Lu, X. Zhao, *J. Am. Chem. Soc.* **2019**, 141, 14981-14986.

[36] M. G. Schwab, B. Fassbender, H. W. Spiess, A. Thomas, X. Feng, K. Mullen, *J. Am. Chem. Soc.* **2009**, 131, 7216-7217.

[37] F. J. Uriberomo, J. R. Hunt, H. Furukawa, C. Klock, M. Okeeffe, O. M. Yaghi, *J. Am. Chem. Soc.* **2009**, 131, 4570-4571.

[38] A. Laybourn, R. Dawson, R. Clowes, J. A. Iggo, A. I. Cooper, Y. Z. Khimyak, D. J. Adams, *Polym. Chem.* **2012**, 3, 533-537.

[39] M. Liu, L. Gan, W. Xiong, Z. Xu, D. Zhu, L. Chen, *J. Mater. Chem. A* **2014**, 2, 2555-2562.

[40] Y. Wan, X. Qian, N. Jia, Z. Wang, H. Li, D. Zhao, *Chem. Mater.* **2008**, 20, 1012-1018.

[41] M. Zhou, F. Pu, Z. Wang, S. Guan, *Carbon*, **2014**, 68, 185-194.

[42] Y. Zhao, M. Liu, X. Deng, L. Miao, P. K. Tripathi, X. Ma, D. Zhu, Z. Xu, Z. Hao, L. Gan, *Electrochim. Acta* **2015**, 153, 448-455.

[43] T. Mendezmorales, N. Ganfoud, Z. Li, M. Haefele, B. Rotenberg, M. Salanne, *Energy Storage Mater.* **2019**, 17, 88-92.

[44] Eftekhari A, *J. Mater. Chem. A* **2018**, 6, 2866-2876.

[45] L. Fan, L. Yang, X. Ni, J. Han, R. Guo, C. Zhang, *Carbon* **2016**, 107, 629-637.

[46] L. Li, E. Liu, J. Li, Y. Yang, H. Shen, Z. Huang, X. Xiang, W. Li, *J. Power Sources* **2010**, 195, 1516-1521.

[47] J. Huang, B. G. Sumpter, V. Meunier, *Angew. Chem*. **2008**, 120, 530-534

[48] A. Borenstein, O. Hanna, R. Attias, S. Luski, T. Brousse, D. Aurbach, *J. Mater. Chem. A*, **2017**, 5, 12653-12672

[49] H. Huang, H. Tan, K. Zou, Y. Deng, G. Chen, *Chem. Commun.*, **2020**, 56, 2182-2185

[50] M. Yang, Z. Zhou, *Adv. Sci.*, **2017**, 4, 1600408

[51] L. Hao, B. Luo, X. Li, M. Jin, Y. Fang, Z. Tang, Y. Jia, M. Liang, A. Thomas, J. Yang, L. Zhi, *Energy Environ. Sci.*, **2012**, 5, 9747

[52] D.Xue, D. Zhu, W. Xiong, T. Cao, Z. Wang, Y. Lv, L. Li, M. Liu, L. Gan, *ACS Sustainable Chem. Eng.*, **2019**, 7, 7, 7024–7034

[53] Y. Lu, J. Liang, S. Deng, Q. He, S. Deng, Y. Hu, D. Wang, *Nano Energy* **2019**, 65, 103993.

[54] L. Wang, D. Shao, J. Guo, S. Zhang, Y. Lu, *J. Solid State Chem.* **2019**, 277, 630-635.

[55] Y. Liu, X. Wang, X. Jiang, X. Li, L. Yu, *Nanoscale* **2018**, 10, 22848-22860.

[56] X. Wei, S. Wan, S. Gao, *Nano Energy* **2016**, 28, 206-215.

[57] N. Diez, R. Mysyk, W. Zhang, E. Goikolea, D. Carriazo, *J. Mater. Chem. A* **2017**, 5, 14619-14629.

The table of contents entry should be 50–60 words long, and the first phrase should be bold.

Coexistence of intramolecular imine (C=N) and aminal bonds in the polymer precursor aids to produce N-doped porous carbon for high-performance supercapacitor.

Keywords
Aminal bonding, activation, nanosphere, porous carbon, supercapacitor

F. Li, X. Huang*, N. Wang, X. Zhu, V. Chan, R. Zhao and Y. Chao*
Corresponding Author*

Title: Aminal/Schiff-Base Polymer to N-doped Porous Carbon Nanospheres for High-Performance Supercapacitor

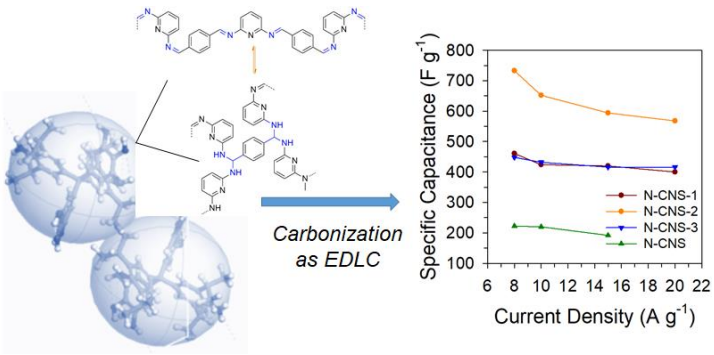

((Supporting Information can be included here using this template))

Supporting Information

Aminal/Schiff-Base Polymer to N-doped Porous Carbon Nanospheres for High-Performance Supercapacitor

Fei Li[1], Xinhua Huang[*,1], Nuoya Wang[1], Xingxing Zhu[1], Vincent Chan[2], Ruikun Zhao[3], Yimin Chao*[*,4]*

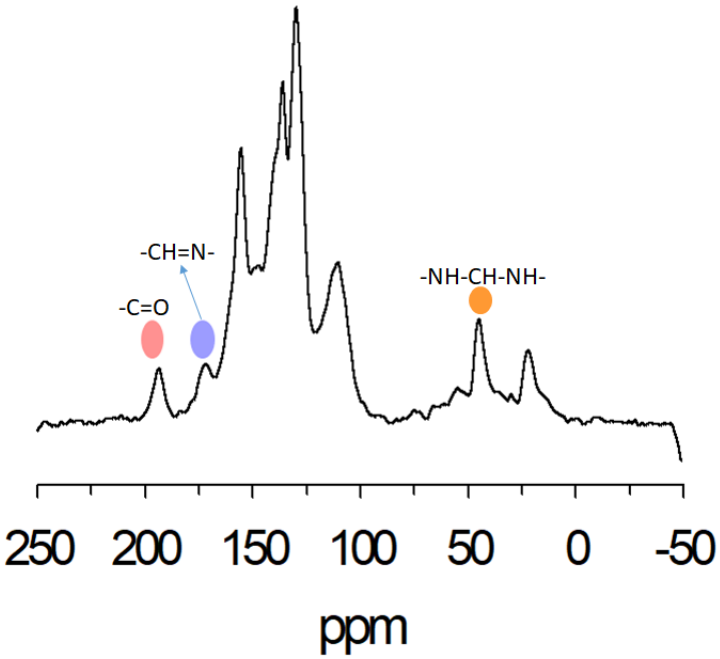

Figure S1. The solid-state ^{13}C NMR spectrum of Schiff-base polymer

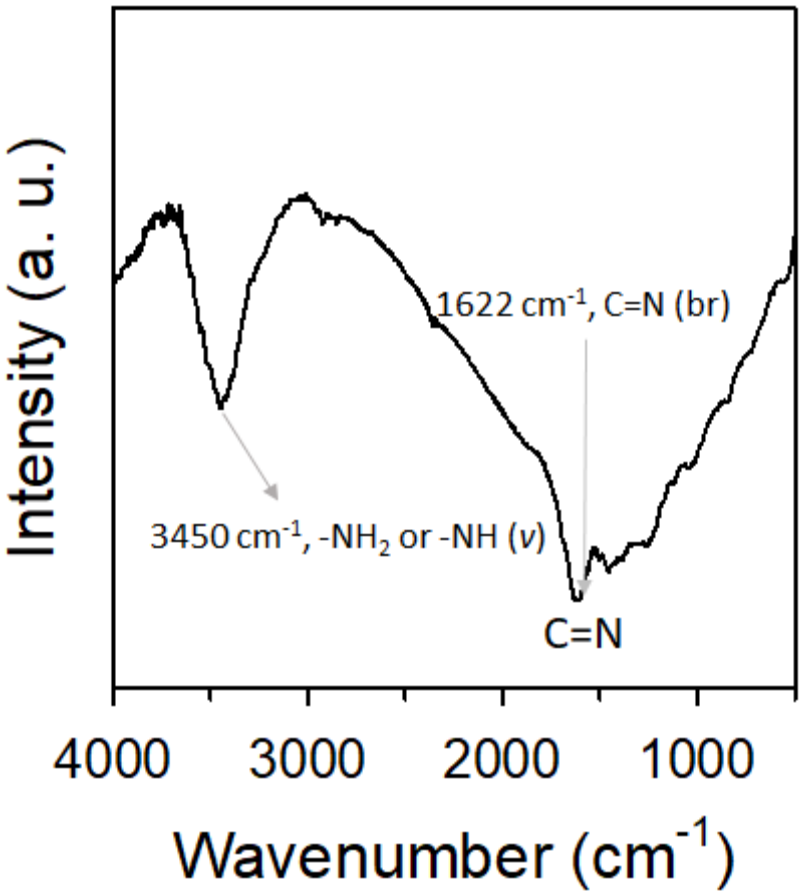

Figure S2. The FT-IR spectra of the Schiff-base polymer.

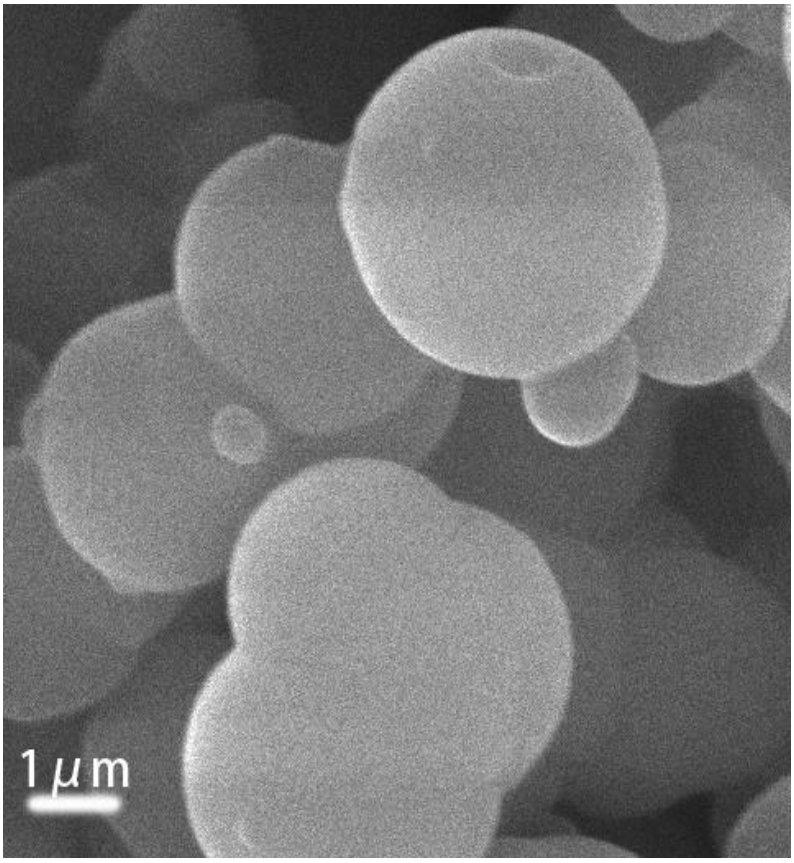

Figure S3. SEM image of polymer before activation

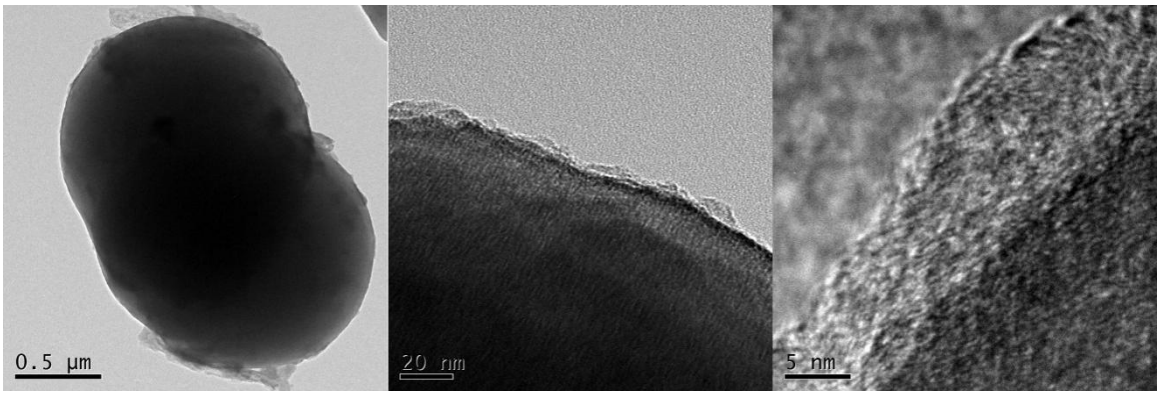

Figure S4. TEM images of N-CNS-2 with different resolution.

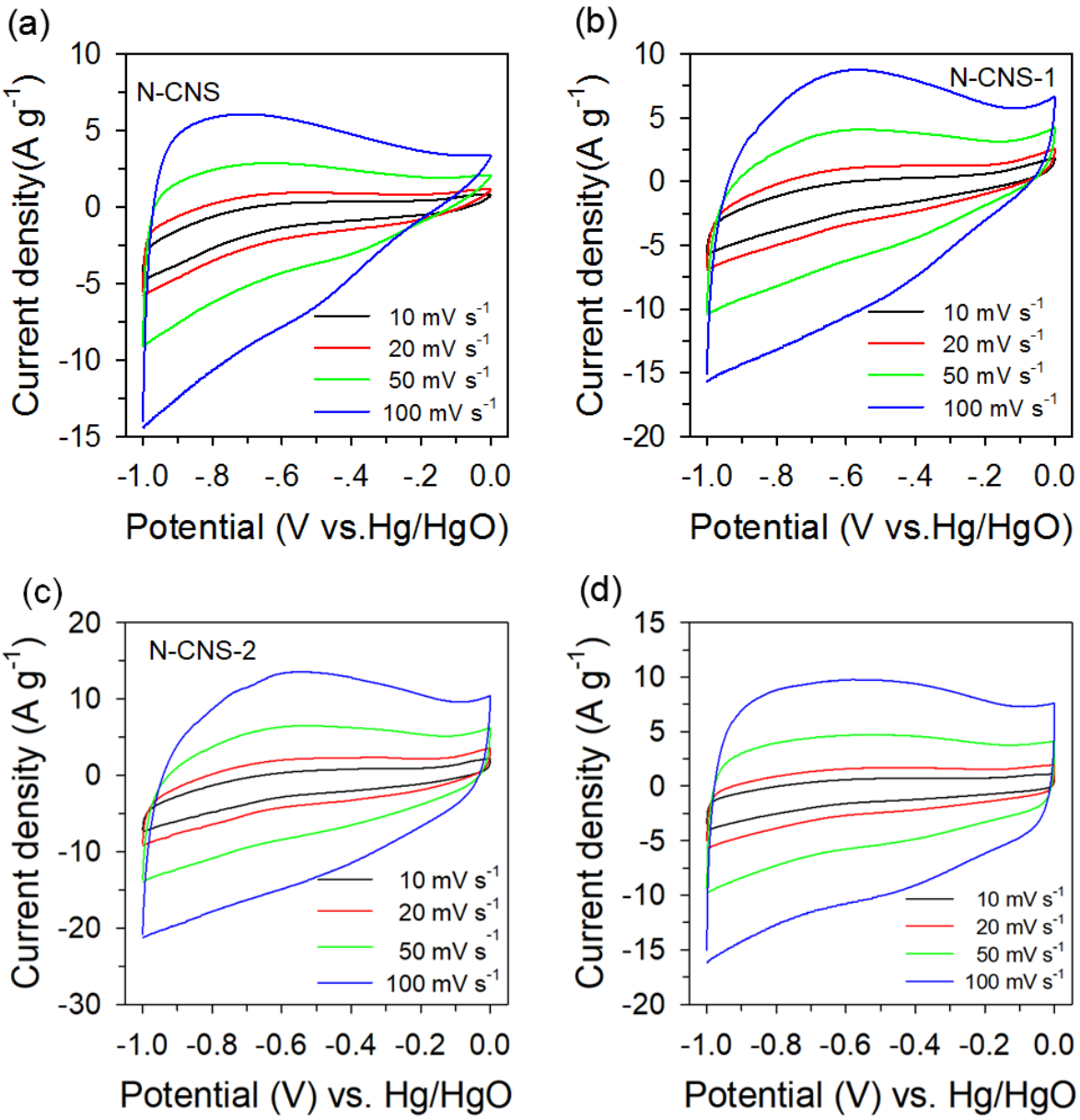

Figure S5. CV curves of all the N-CNS electrodes at different scan rate.

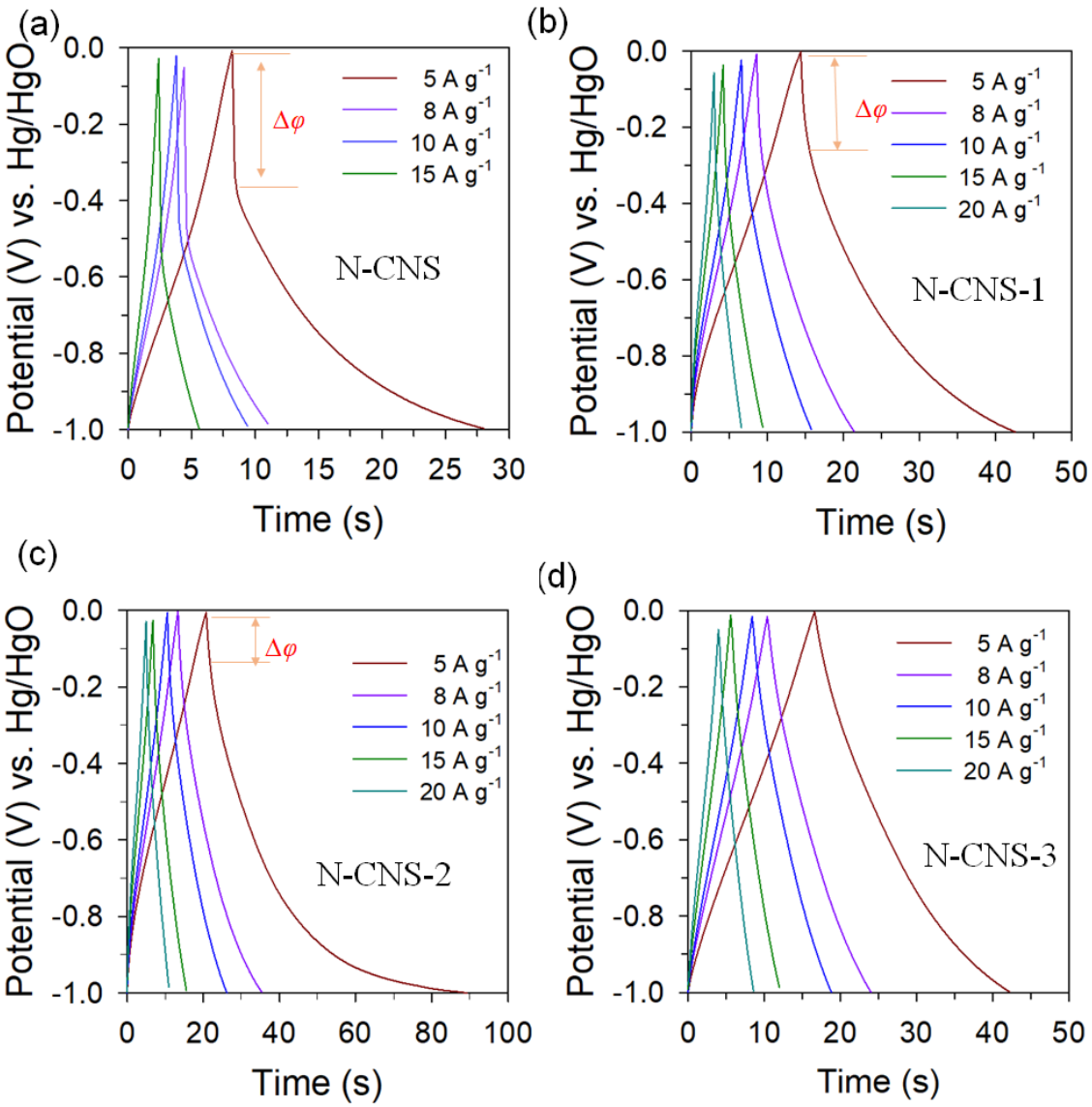

Figure S6. GCD curves of all the N-CNSs electrodes at different current density.

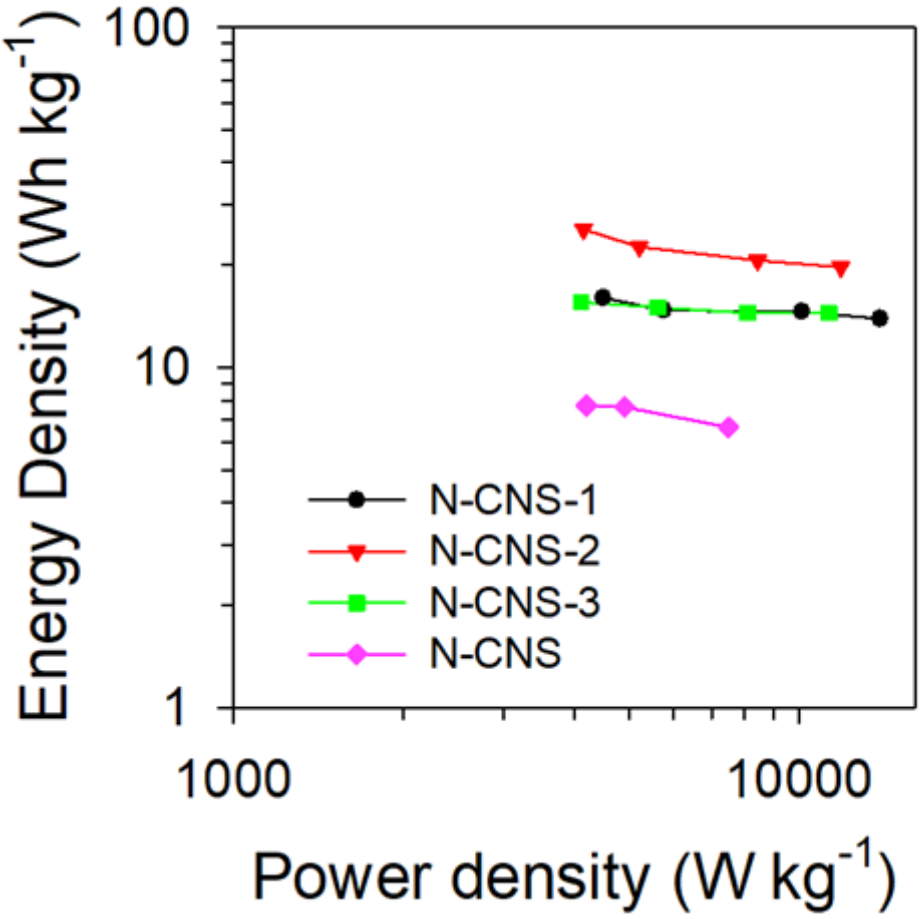

Figure S7. The Ragone plots of the N-CNSs (energy density vs. power density) at different current density (8, 10, 15 and 20 A g^{-1})